



HAL
open science

Damage in Armor Ceramics Subjected to High-Strain-Rate Dynamic Loadings: The Spherical Expansion Shock Wave Pyrotechnic Test

Antonio Cosculluela, Pascal Forquin

► **To cite this version:**

Antonio Cosculluela, Pascal Forquin. Damage in Armor Ceramics Subjected to High-Strain-Rate Dynamic Loadings: The Spherical Expansion Shock Wave Pyrotechnic Test. Handbook of Damage Mechanics; Nano to Macro Scale for Materials and Structures, Springer New York, pp.1-30, 2021, 10.1007/978-1-4614-8968-9_81-1 . hal-04470637

HAL Id: hal-04470637

<https://hal.univ-grenoble-alpes.fr/hal-04470637>

Submitted on 21 Feb 2024

HAL is a multi-disciplinary open access archive for the deposit and dissemination of scientific research documents, whether they are published or not. The documents may come from teaching and research institutions in France or abroad, or from public or private research centers.

L'archive ouverte pluridisciplinaire **HAL**, est destinée au dépôt et à la diffusion de documents scientifiques de niveau recherche, publiés ou non, émanant des établissements d'enseignement et de recherche français ou étrangers, des laboratoires publics ou privés.

Handbook of Damage Mechanics; Nano to Macro Scale for Materials and Structures

Second Edition

DAMAGE IN ARMOR CERAMICS SUBJECTED TO HIGH STRAIN-RATE DYNAMIC LOADINGS. THE SPHERICAL EXPANSION SHOCK WAVE PYROTECHNIC TEST.

Antonio Cosculluela^{1*}, Pascal Forquin²

¹CEA-CESTA, 15 avenue des Sablières, CS 60001, 33116 Le Barp Cedex 1, France,
antonio.cosculluela@cea.fr

²Univ. Grenoble Alpes, Grenoble INP, CNRS, Laboratoire 3SR, BP53, 38041 Grenoble Cedex 9, France,
pascal.forquin@univ-grenoble-alpes.fr

*Corresponding author

Abstract

For shielding type or armor applications, it is important to know the state of the material well after the passage of the divergent spherical wave which comes off in front of the impactor projectile. The objective of this chapter is to present an experimental technique which make it possible to load materials in a large range of dynamic strain and stress: The Spherical Expansion Shock Wave Pyrotechnic Test. The paths of loading, the observed micro-physical phenomena and the associated behaviors of two brittle materials (two ceramics) are described. A particular focus is made on the influence of the microstructure and the nature of the ceramic on their dynamic behavior. Numerical simulations are presented. Some of them give the history of the states of strain and stress as well as contribute to the understanding of the physical phenomenology; the others report on the experimental mechanical behavior of these ceramics. This chapter show that is important to consider the state of the material after being submitted to an initial divergent spherical wave before modelling the mechanical response of the material in a shielding type structure. These analyses allow to better consider physical phenomena in the mechanical behavior modelling and so the improvement of the mechanical strength/density ratio of the constituent materials of these kind of structures.

Keywords: Alumina, Divergent spherical wave, Dynamic behavior, High-strain-rate, Microplasticity, Microcracks, Spherical expansion shock wave pyrotechnic test

Handbook of Damage Mechanics; Nano to Macro Scale for Materials and Structures

Second Edition

1 Introduction

In the context of armor system design, the main goal of material selection whatever their type (plastics, glasses, composites, ceramics...) often boils down to a double technical challenge: mass reduction and increase of performances, especially in the manufacturing of mobile structures (space shuttle, aircraft, armor tanks, helicopters, automotive industry) and personal armor systems. This results in a permanent search to improve the mechanical strength/density ratio of the constituent materials of these structures.

In the case of shielding used against light to heavy caliber Armor-Piercing (AP) projectile, polycrystalline ceramics are of particular interest because they combine qualities of lightness and high mechanical performances in compression. During an impact, in the first moments of the interaction between a projectile and a ceramic shield, a divergent precursor spherical wave originates and propagates in the ceramic structure. In some cases of very light armor built with a ceramic front plate of small thickness, the mass and velocity of the projectile generate a too low energy and stress level. In this case, the study can rather focus on the structural response of the shield backing.

Conversely, in the other cases, the stresses increment induced by the precursor wave can alter the ceramic due to microplasticity and tensile damage mechanisms and change the subsequent structural response of the shield. It is therefore essential to first investigate all the physical changes induced by this wave.

The objective of the present chapter is a contribution to the phenomenological study of the damage modes induced in ceramic materials by a divergent spherical wave (explosive test). In particular, the influences of the stress field, the stress rate and the microstructural parameters are studied. A special focus to the influence of material parameters (flaws, grain size) is given. The description and understanding of the physical phenomena aim to provide the basis of mechanical models that may constitute the purpose of a future study. The outline of the present chapter is dictated to the use of Spherical Expansion Pyrotechnic tests. The structural response of the shield is outside of the scope of this chapter.

This chapter contributes to the identification of macro and micro-phenomena observed in two types of alumina during a divergent spherical wave loading. This chapter exhibits some microscopic results too. SEM and TEM observations illustrate the physical phenomena that are involved in the response of these materials loading by a divergent spherical wave. The two studied ceramic grades are 99.7% pure alumina with coarse-grained and fine-grained microstructures. The grain size is observed to be an essential microstructural parameter in the mechanism of cracking and ruin of alumina under divergent spherical wave loading.

2 Description of the problem

The framework of this chapter is the investigation of the damage processes that precede the subsonic penetration of an armor-piercing projectile impacting a heavy armor ceramic. If ones consider the

Handbook of Damage Mechanics; Nano to Macro Scale for Materials and Structures

Second Edition

interaction between a high-intensity aggression (AP projectile, medium-caliber projectile, arrow projectile, hollow charge) and a heavy ceramic shield, in the first moments of the interaction, a divergent precursor spherical wave originates at the point of impact and propagates in the ceramic structure. In the particular case of arrow projectiles or hollow charges the typical impact velocities are respectively $1,500 \text{ m.s}^{-1}$ and $9,000 \text{ m.s}^{-1}$ and the kinetic energies are of the order of 5 MJ; the stresses conveyed by the diverging precursor spherical wave go up to a few tens of GPa. The penetration rates reach from 500 m.s^{-1} (arrow projectiles) to $3,000 \text{ m.s}^{-1}$ (shaped charge ; https://fr.qaz.wiki/wiki/Shaped_charge). Given the propagation speed of the precursor wave of the order of $10,000 \text{ m.s}^{-1}$, it means that the stress wave have enough time to modify the ceramic before the penetrator interacts with the ceramic. In addition, the stress values are such that they can cause microstructural modifications of the ceramic.

In the cases of light and medium caliber Armor-Piercing (AP) projectile, the physical phenomenon is the same but the energy and the stresses level are lower. The different states of stress experienced by an isolated volume element of a ceramic shielding plate are illustrated in the Figure 1. At time t_1 , the precursor spherical wave has detached itself in front of the projectile but has not yet reached the considered volume element. At time t_2 , the wave interacts with this volume element which then undergoes a triaxial compression state corresponding to a uniaxial strain loading-path. Then, when the wave front moves away, the material relaxes and the stress state becomes uniaxial compression (time t_3) before reaching a state of compression biaxial tensile state (t_4). Given the brittle nature of ceramics, this state of biaxial tensile state generates a tensile damage in the material. It is therefore scientifically legitimate to be interested in the modifications (such as plasticity, damage and cracking mechanisms) made by the precursor wave to the material in order to predict the state of the latter before it interacts with the projectile. In this perspective, this work consists in studying the mechanical behavior of ceramics loading by a divergent spherical wave can be studied.

Figure 2 shows the loading path, in the stress space, imposed on an elastic material by a divergent spherical longitudinal wave. The compression is taken as positive. This loading is complex insofar as it involves a sequence of states of different stresses. If the state of the material changes during the loading (plasticity, damage, for example), then, at a given moment, the response of the material depends on the state of stresses but also on the history of the previous states of stresses.

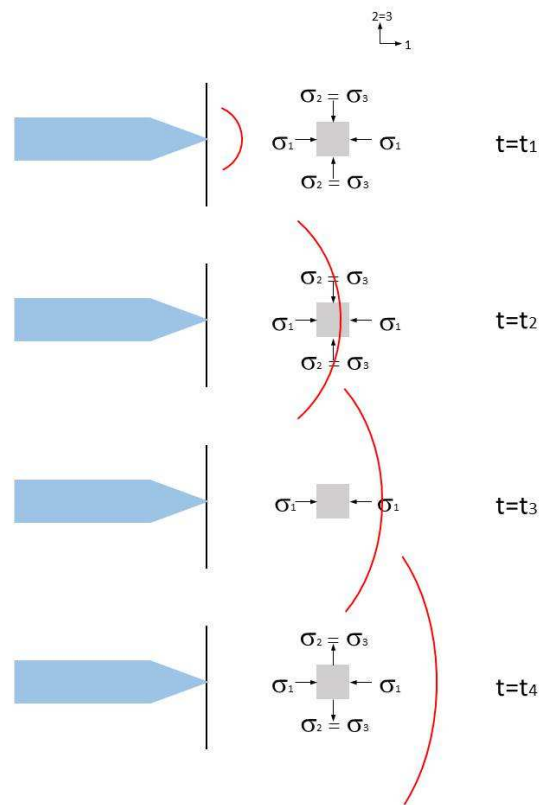


Fig. 1 States of stresses imposed on an element of volume by a divergent spherical wave

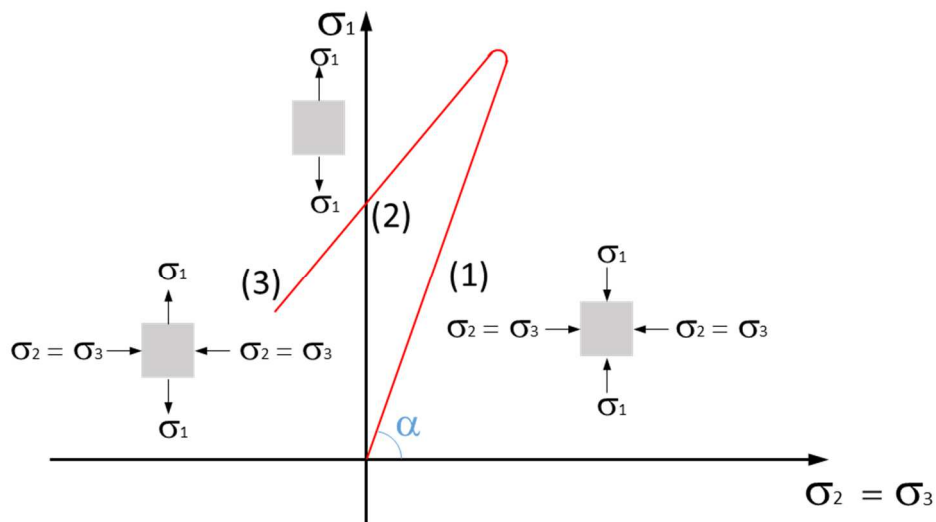


Fig. 2 Loading path imposed by a divergent spherical wave to an elastic material

Handbook of Damage Mechanics; Nano to Macro Scale for Materials and Structures

Second Edition

It is therefore necessary to identify the behavior of materials at various stages to reconstruct the history of its response; so, it is possible to integrate for a given stage the modifications of the materials of the previous stage.

To better understand the interest in carrying out divergent spherical wave loading tests (Coscolluela 1992) or edge-on impact tests (Forquin et al. 2003), it is necessary to more explain the figure 2. This figure, established from numerical simulations presented below in chapter 4, shows, the loading path imposed by a divergent spherical longitudinal wave to a material whose behavior remains elastic in this example.

Let's detail the different phases of this complex loading:

- The compression phase takes place in a state of uniaxial strain (1). The strain rates involved in the stage are of the order of 10^5 s^{-1} .
- A relaxation phase passes through the axis of uniaxial compression (2) (Cagnoux et al. 1991a; 1991b), and then the material undergoes compression-bitension (3). The strain rates involved are of the order of 10^3 s^{-1} to 10^4 s^{-1} .

In order to investigate the damage and deformation modes of the component material in situ, experiments allowing the identification of the response material for different states of stress must be carried out. Experiments developed to recreate this stress-state using an explosive (Coscolluela 1992) or using Edge-On-Impact tests (Forquin et al. 2003; Riou et al. 1998) can be performed.

3 State of the art and position of the problem for the divergent spherical wave test

The interaction of a spherical divergent wave and a brittle material has been studied for a long time (Blake Jr. 1952; Ghosh 1969); some studies focused on ceramics (Bless et al. 1990; Evans and Fu 1984; Satapathy 2001) and rare studies focused on microstructural aspects (Louro and Meyers 1989; Howitt and Kelsey 1988; Coscolluela 1992).

The purpose of this subsection is to exhibit the response of two sintered aluminas loaded by a divergent spherical wave and to show the influence of the grain size on the induced mechanisms and their mechanical behavior.

Figure 3 shows the loading path imposed on an elastic material by a spherical longitudinal divergent wave. Compared to classical uniaxial compressive strain and uniaxial compressive stress test, this kind of experimental procedure explores a new domain in the space of stresses, located between the axis of uniaxial strain and the axis of uniaxial tensile stress. So, if new phenomena appear, they would be then attributed to the new stress states. The divergent character of the spherical wave makes it possible to impose on different sub-volumes of the same sample, a different history of stresses (figure 3).

Handbook of Damage Mechanics; Nano to Macro Scale for Materials and Structures

Second Edition

In this chapter, the phenomenology of the behavior is associated with the history of radial stress. To do so, post-test analyses are carried out. Fragments collected at different abscissas, after the passage of the wave, are observed at macro and microscopic levels. Next, these observations are connected to the measurements made at the same abscissa. Before that and to facilitate the interpretation of the measurement results, some numerical simulations of the experiments are carried out.

This subsection is therefore structured as follows: in a first time, the results of numerical simulations are presented. Next, in a second step, the measurements are provided. Finally, the observations made on each alumina at the end of the recovery tests are commented. Finally, the last part is devoted to discussion.

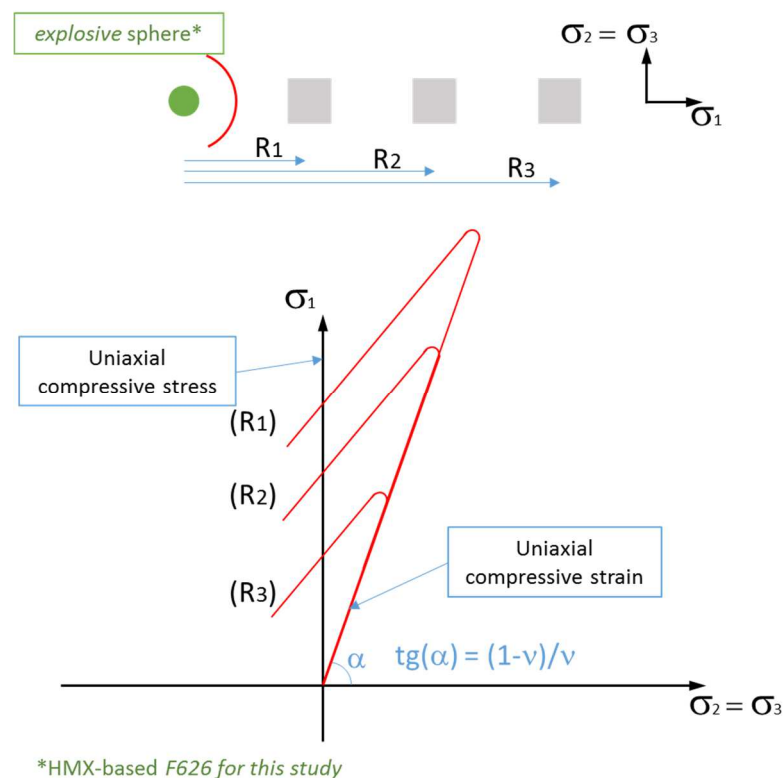


Fig. 3 Loading path applied to a material loading at three different abscissas

4 Numerical investigation of the loading history

A Lagrangian one-dimensional explicit code (EPIC) is used to simulate the divergent spherical wave test. This code is based on a finite difference scheme and therefore specially designed for wave propagation problems. The explosive, the alumina sample and a PMMA window are meshed using mesh made of 500 1D finite-elements. The behavior of alumina is elastic in a first simulation, then perfectly plastic elastic in a second simulation.

Handbook of Damage Mechanics; Nano to Macro Scale for Materials and Structures

Second Edition

Assumptions for numerical simulations are that the geometry is 1D, the pressure is not measured in contact with the explosive, so the stress level is chosen with theoretical calculations on F626 explosive. Regarding the material constitutive behavior, two cases are considered: in the first calculation, the material behavior remains elastic whereas in the second calculation a yield stress equal to 3.5 GPa with a perfect plastic behavior is used. The density of the material is 3.92 and the Young modulus is 380 GPa.

4.1 Elastic behavior hypothesis

In the case of elastic behavior, the waves are elastic waves, not shock waves because shock waves occur when a material is stressed far beyond its elastic limit by a pressure disturbance. All the particle velocity profiles have the same shape, with a steep rise, a maximum and a decrease.

The decrease of the maxima is of type $1/r$ in accordance with the closed-form solution proposed by Rinehart (1975). Furthermore, the same author also specifies that, on the rising edge, the radial stress is proportional to the radial particle velocity u_r , the mass density ρ and the longitudinal wave celerity C_L :

$$\sigma_r = \rho C_L u_r \quad (\text{Eq. 1})$$

After the maxima and during stress relaxation, the particle velocity $u_r(r, t)$ depends on the radial stress $\sigma_r(t)$, the radius r (abscissa of the figure 3), and the longitudinal wave velocity C_L :

$$u_r(r, t) = \frac{\sigma_r(t)}{4G} \left[\left(\frac{a}{r^2} \right) - \sqrt{\frac{3a}{2r^2}} e^{-\omega t/\sqrt{2}} \sin(\omega t + \tan^{-1}\sqrt{2}) + \sqrt{2} \frac{a}{r} e^{-\omega t/\sqrt{2}} \sin \omega t \right], \quad (\text{Eq. 2})$$

where

$$\omega = 2\sqrt{2} C_L/3a \quad (\text{Eq. 3})$$

For elastic behavior, some relationships exist between the elastic parameters of a material and the wave velocities, and between its different elastic parameters:

$$C_L = \sqrt{\frac{K+4/3G}{\rho}} \quad (\text{Eq. 4})$$

$$C_s = \sqrt{\frac{G}{\rho}} \quad (\text{Eq. 5})$$

$$C_0 = \sqrt{\frac{K}{\rho}} \quad (\text{Eq. 6})$$

$$C_b = \sqrt{\frac{E}{\rho}} \quad (\text{Eq. 7})$$

$$E = 2\mu(1 + \nu) = 3K(1 - 2\nu) = \frac{\mu(3\lambda + 2\mu)}{\lambda + \mu} = \frac{9\mu K}{3K + \mu} \quad (\text{Eq. 8})$$

$$G = \mu = \frac{E}{2(1 + \nu)} = \frac{3K(1 - 2\nu)}{2(1 + \nu)} = \frac{3EK}{9K + E} \quad (\text{Eq. 9})$$

$$K = \frac{E\mu}{9\mu-3E} = \frac{E}{3(1-2\nu)} = \frac{3\mu(1+\nu)}{3(1-2\nu)} = \frac{2\mu}{3} + \lambda \quad (\text{Eq. 10})$$

$$\nu = \frac{\lambda}{2(\lambda+\mu)} = \frac{3K-E}{6K} = \frac{3K-2\mu}{2(3K+\mu)} = \frac{E}{2\mu} - 1 \quad (\text{Eq. 11})$$

$$\lambda = \frac{(E-2\mu)\mu}{3\mu-E} = \frac{E\nu}{(1+\nu)(1-2\nu)} = \frac{3K(3K-E)}{9K-E} = \frac{2\mu\nu}{1-2\nu} = K - \frac{2\mu}{3} = \frac{3K\nu}{1+\nu} , \quad (\text{Eq. 12})$$

where E is the Young's modulus, G the Shear modulus, K the Bulk modulus, ν the Poisson's ratio, λ and μ the Lamé's parameters ($G = \mu$), C_L is the longitudinal wave velocity, C_s the shear wave velocity, C_0 the bulk wave velocity and C_b the rod wave velocity.

The divergent spherical expansion is simulated considering, first, a purely elastic behavior for the ceramic material. Figure 4 shows the profile of radial stress as function of the orthoradial (hoop) stress for different abscissas. The maximum radial stresses reached for abscissa 22 mm, 30 mm, 50 mm and 70 mm are respectively 35, 32, 23, 12 and 8 Mpa. An elastic perfectly plastic behavior is considered for the ceramic material in the next subsection.

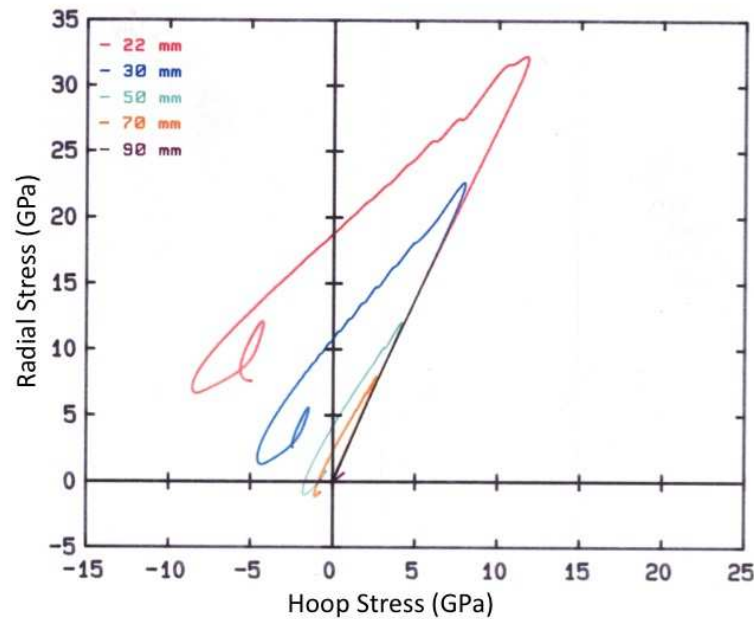


Fig. 4 Numerical simulation of the loading path imposed by a divergent spherical wave to an elastic material

4.2 Elastic perfectly plastic behavior hypothesis

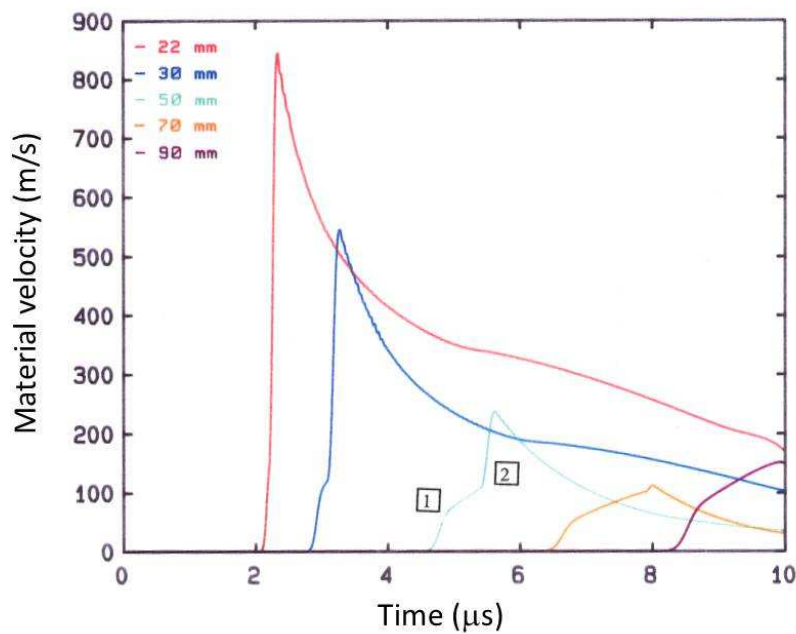
Figure 5a and 5b show the profiles of particle velocities and radial stresses for different radii. The history of stresses is presented in the main stresses space (Fig. 5c). The abscissa considered is the same than in

Handbook of Damage Mechanics; Nano to Macro Scale for Materials and Structures

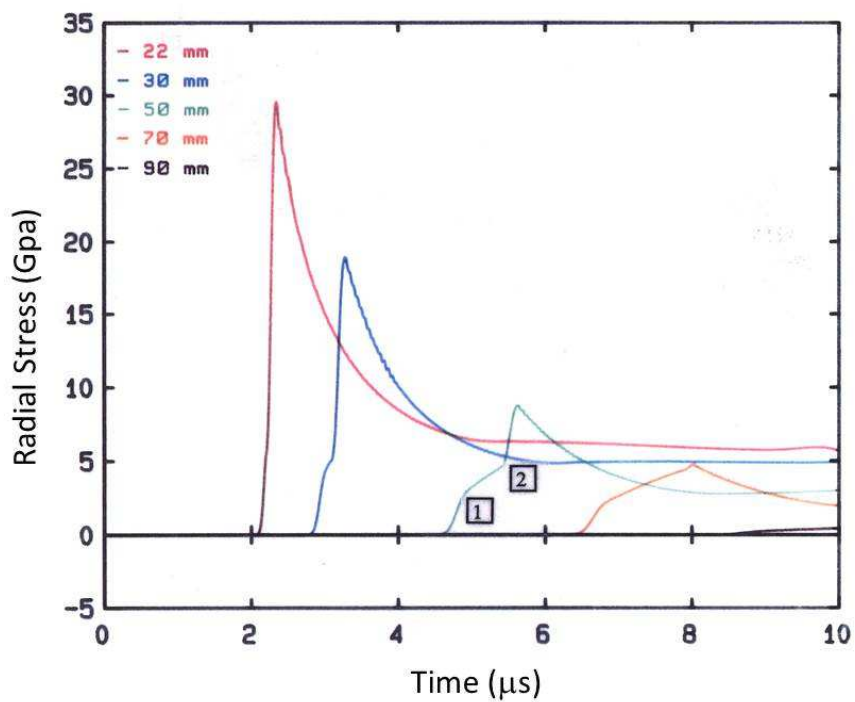
Second Edition

the previous subsection. The maximum radial particle velocities are respectively: 850 m/s, 552 m/s, 240 m/s, and 111 m/s.

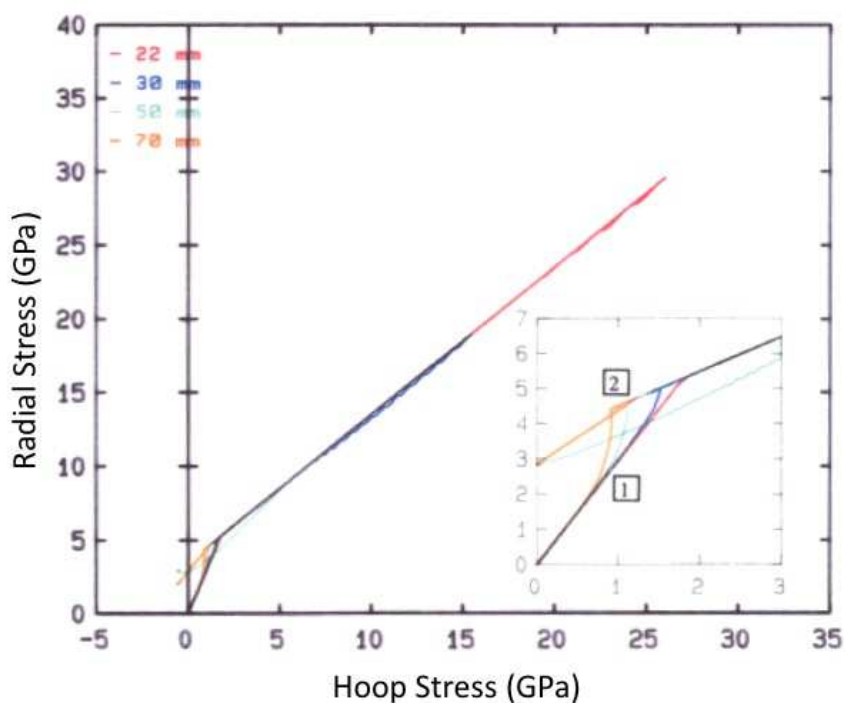
All these profiles exhibit a detachment of an elastic precursor. The greater the distance of propagation the more marked this detachment. Level of this precursor also decreases with the propagation distance. So, it cannot be considered as an intrinsic parameter of the material, yet it is significant of the alumina behavior change. Figure 5c raises this paradox. Indeed, this figure shows that the change in slope of the elastic precursor [1] corresponds to the moment when the loading path leaves the uniaxial strain axis. The arrival of this route on the plasticity criterion (von Mises cylinder) induced on the material velocity profile a second wave front [2]. The elastic precursor level slightly decreases with the increase of the distance from the center of the explosive radius.



(a)



(b)



(c)

Fig. 5 Numerical simulation of a divergent spherical wave considering an elastoplastic behavior for the ceramic material. (a) Radial particle velocity versus time, (b) Radial stress versus time, (c) Radial stress versus hoop stress.

5 Experiments performed on two alumina ceramics

The numerical simulations presented in the previous paragraph can help us to exploit and interpret the experimental results. Before that, the studied materials are introduced hereafter.

5.1 Presentation of the two alumina ceramics

The processes for making sintered alumina are diverse. For making the two studied alumina, the main following steps are completed:

- choice of one or more alumina powders,
- production of a manipulable mixture,
- pouring, spinning or pressing the mixture so as to obtain the raw,
- machining, if necessary, of the raw material according to the type of part manufactured,
- raw cooking: sintering cycle with or without pre-sintering cycle,
- machining of the cooked parts according to the tolerances required on the final product.

The main production parameters of each studied alumina are described hereafter.

The alumina AL23 is manufactured by the company DEGUSSA France. The applied uniaxial stress is around 100 MPa. The slip is dried, pressed and then cooked. The parts are then sintered without additions. The sintering temperature is 1780°C. The maximum temperature level is two hours. The density is about 3.92. The grain size distribution is between 10 and 50 microns.

The alumina T299 is manufactured by the company ALCOA France. This alumina is obtained by cold isostatic pressing at a pressure of 150 MPa. Initial powder contains 2% acrylic binder. The role of the binder acrylic is to give cohesion to the grains during the atomization process. This process consists of granulating the powder. The parts are then sintered without additions. The sintering temperature is 1600°C. The density is about 3.86 and the grain size distribution is between 1 and 20 microns.

The table 1 provides some acoustic and mechanical properties of the two studied alumina.

Handbook of Damage Mechanics; Nano to Macro Scale for Materials and Structures

Second Edition

Table 1 Physical properties of materials used in this experimental study (uncertainties: 7%)

Physical property	Alumina AL23	Alumina T299	Polymethyl methacrylate PMMA
Longitudinal wave speed (m/s)	10 800	10 300	-
Shear wave speed (m/s)	6200	6100	-
Density (-)	3.86	3.85	1.19
Young Modulus (GPa)	380	353	13
Poisson Ratio (-)	0.26	0.23	-
Mean grain size (μm)	40	5	-
Purity (%)	99.7	99.6	-

5.2 Experimental set-up and instrumentation

For each material described above, several cylindrical blocks are machined with a good surface finish to bond window material; the particle velocity measurements are carried out using a DOPPLER-LASER interferometry chain (IDL). This means makes possible to measure the particle velocity on a free surface or at an interface (with a PMMA window material) with an accuracy of the order of 1% and a temporal resolution of the order of 10 ns. Its operating principle is the same than that of VISAR (Velocity Interferometer System for Any Reflector). Figure 6 describes the experimental set-up.



Fig. 6 Experimental set-up dedicated to the material velocity measurements at the rear face of the material loaded by a divergent spherical wave

Alumina blocks are finely machined. A hemispherical cavity is machined at the center of each block. This cavity is used to place the explosive (HMX based F626). The explosive is machined into a hemispherical shape and is initiated in the middle of the flat part; thus a divergent spherical wave is generated. The window material is made of PMMA because it has a refractive index roughly constant as function of the applied pressure. The window is polished and metallized with gold. Its center is located thanks to four bands made on the metallization.

This window is centered and glued with a slow araldite on the rear face of the alumina block. The whole set-up rests on a PVC (polyvinyl chloride) ring. The laser beam is in turn centered thanks to a ferrule oriented by two micrometric screws. This centering operation is very important because it conditions the validity of the measurement.

5.3 Experimental results obtained with coarse-grained alumina AL23

Figure 7 shows the measured velocity profiles at the alumina-PMMA interface. The distance between the center of the explosive and the measuring points depends on the size of the block of alumina. The recorded profiles present a similar shape compared to the material velocity profiles obtained from numerical simulations (Figure 5a). However, an improvement of the constitutive law is recommended.

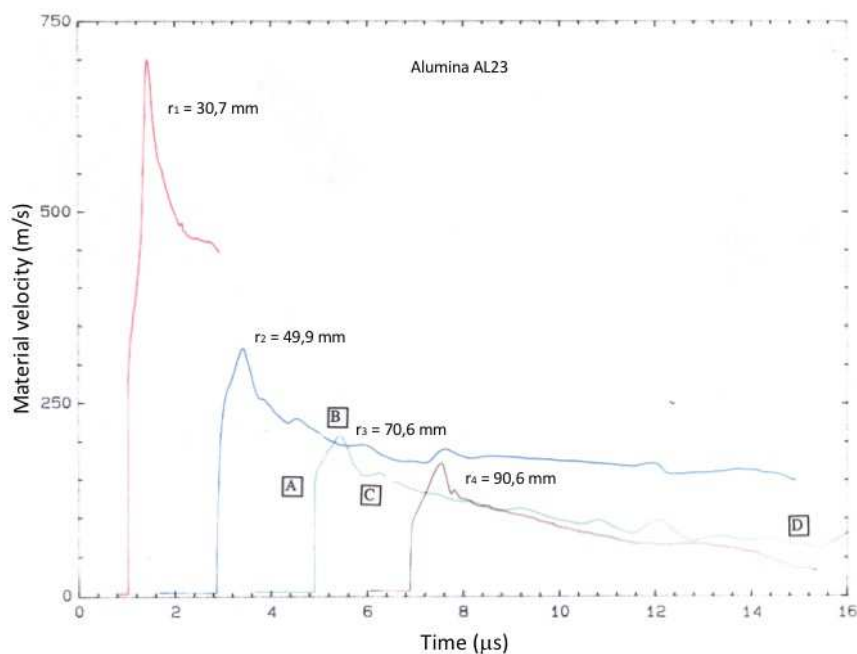


Fig. 7 Velocity profile at the AL23 alumina-PMMA interface for different distances from the center of the detonation

The presence of an elastic precursor is noted. The slope discontinuity [A] corresponds to the moment when the material ceases to be in a state of uniaxial strain. The decrease in velocity peaks [B] is a function

Handbook of Damage Mechanics; Nano to Macro Scale for Materials and Structures

Second Edition

in $1/r$ (r = radial distance to the explosive center). However, the plastic wave detachment is not clearly observed. This is related to the viscous nature of plastic strain (Coscolluela, 1992). So, in the case of alumina, as in uniaxial strain loading (plate impact), detachment of the plastic wave does not appear as a divergent spherical wave.

With regard to the mitigation of the material velocity profiles (figure 7), they are composed of an exponential decrease ([B] to [C]), followed by an almost straight part ([C] to [D]). The shape of the unloading, can be compared to the shape of the velocity profiles obtained by numerical simulation in the perfectly plastic elastic case (figure 5a). It is supposed that this mitigation is related to plastic phenomena although, on the other hand, only the almost straight part ([C] to [D]) would account for the multiple-cracking of the blocks. Indeed, this cracking phenomenon seems to have damping effect on the release.

It's difficult to properly exploit these velocity profiles to identify the state of stresses as it could be done in the case of plate impact tests or in the case of the impact against a long bar.

5.4 Experimental results obtained with fine-grained alumina T299

The stacking of T299 alumina discs allowed performing IDL measurements at different radii as in the case of alumina AL23. On the other hand, in addition to these material velocity measurements, stress and strain measurements are performed by using gauges glued between the discs. The glue used is a slow araldite. Here again, several abscissas are instrumented. These measurements are made using of manganin/constantan gauges. When this gauge inserted in-between the discs is pressured by a divergent spherical longitudinal stress wave, the reaction of the manganin frame causes an increase in its resistance due to the piezo resistivity of the manganin. This frame also undergoes elongation from the unevenness of the shock wave. It is the sum of these two effects which is measured by recording the change of resistance of the manganin frame during the passage of the stress wave. As the constantan frame is bounded to the manganin, the levels of stress and elongation is the same. Unlike manganin, constantan is little piezo resistive, so its reaction is mainly provided by the elongation of its frame. This double measurement ("DOPPLER-LASER interferometry chain" and manganin/constantan gauges) allows us to control the validity of gauge measurements from IDL measurements (Coscolluela 1992).

Figure 8 shows the velocity profiles at the alumina-PMMA interface. Again, the distance between the explosive center to the measuring point depends on the size of the block of alumina. The obtained profiles have a similar appearance to those derived from numerical simulations (figure 5a).

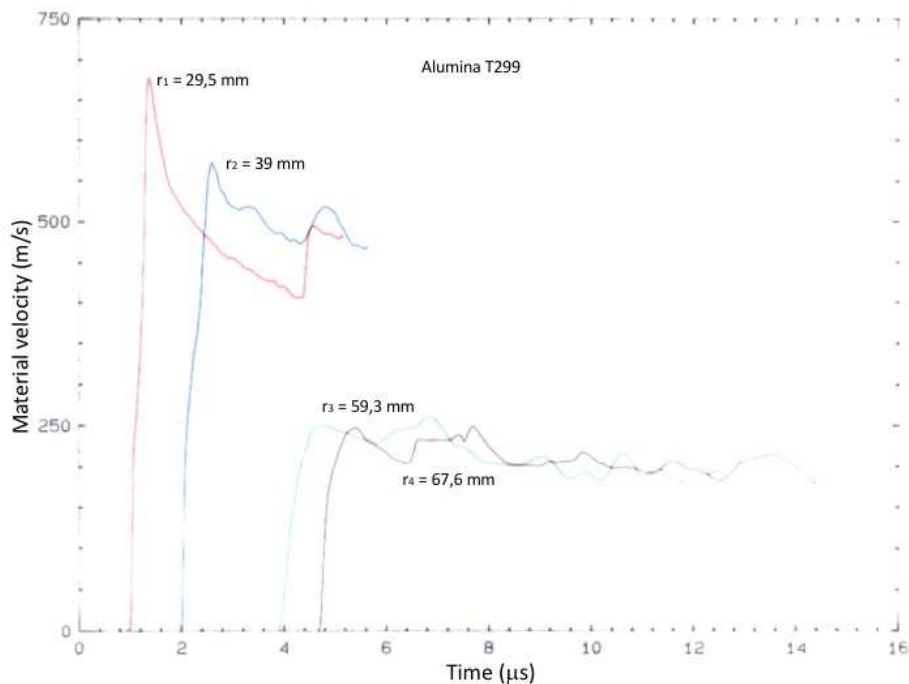


Fig. 8 Profile of the T299 alumina-PMMA interface velocity for different distances from the center of the detonation

Nevertheless, some differences are noted with the ones obtained with coarse-grained alumina. The rise times of elastic precursors are higher. The decrease in particle velocity peaks is less regular. These profiles do not show a clear plastic wave detachment. So, the compression behavior is supposed to differ to that of coarse-grained alumina. On the other hand, the appearance of the detents shows a different behavior between both aluminas.

The authors draw attention on the following remark: apart from the measurement made near the explosive, these other velocity profiles come from a stack of discs. Special care has been taken for the centering of the measurement location. The plates are glued. However, some studies show some issues experienced when divergent spherical wave is encountering an interface, even of identical material. These problems have been raised theoretically by (Rinehart 1975) and experimentally by (Heuze et al. 1991). Their results suggest that, during the compression phase, the particle velocity profiles can be used with confidence, but for the expansion phase, the profiles must be used with caution; the ideal is to model each experiment as properly as possible.

For fine-grained and coarse-grained aluminas, the estimated maximum values of radial stress are calculated from Equation (1) in which the particle velocity takes into account the difference of acoustic impedance between the PMMA and the alumina ceramic. (table 2). These values can then be compared to those obtained by using manganin-constantan gauges (figure 9).

Handbook of Damage Mechanics; Nano to Macro Scale for Materials and Structures

Second Edition

Table 2 Maximal values of alumina-PMMA interface velocity and estimated associated stresses (uncertainties:15%)

Material	Measurement abscissa (mm)	Maximum material velocity (m/s)	Estimated Maximum Stress (GPa)
AL23	30,7	700	15
AL23	49,9	320	7
AL23	70,6	205	4,4
AL23	90,6	185	3,5
T299	29,5	680	15
T299	39	570	12,5
T299	59,3	260	5,7
T299	67,6	248	5,4

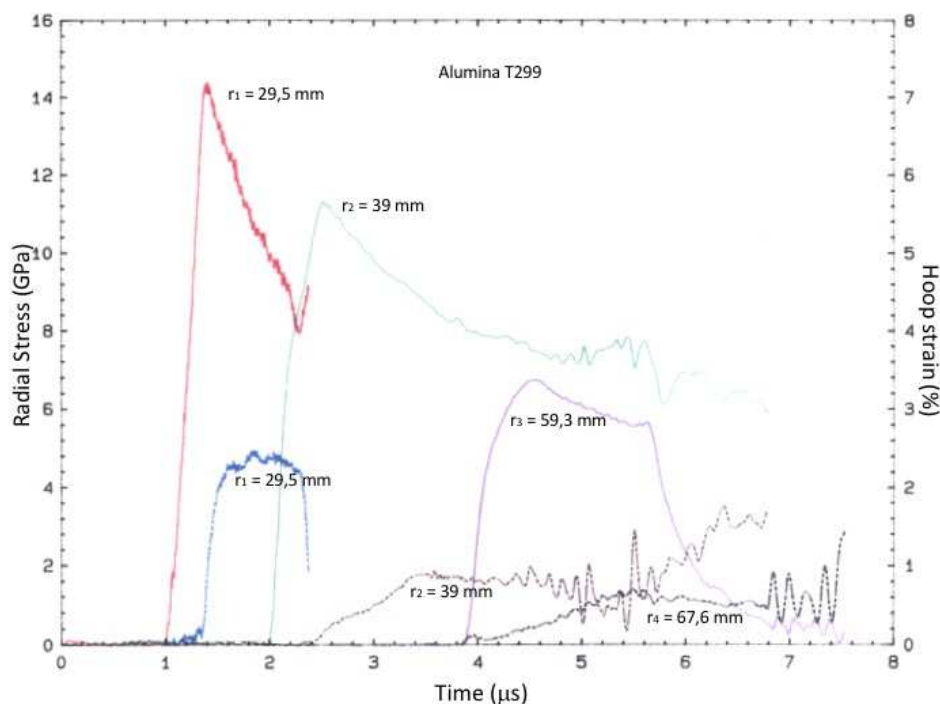


Fig. 9 Profile of the radial stress for different distances from the center of the detonation

As previously explained, the gauges measurements allow us to know the history of the radial stress and the hoop (orthoradial) strain (figure 9). All signals are shifted in time to be compared. During the compression phase, hoop strains remain nil. This is consistent with the fact that this compression phase corresponds to a uniaxial-strain loading. It can also be noted that characteristic signals of small hoop strains are disturbed. That said, they could be used as part of a Lagrangian analysis. The maximum values of radial stress given by the manganin frame are slightly different from those calculated from the interface particle velocity profiles. This difference increases when the measurement abscissa is far from the

Handbook of Damage Mechanics; Nano to Macro Scale for Materials and Structures

Second Edition

explosive. The material velocity measured at $r = 59.3$ mm and $r = 67.6$ mm seems to be underestimated because the stress wave crosses several alumina interfaces before reaching the measuring point.

5.5 Discussion on the experimental results

Material velocity measurements are carried out with DOPPLER-LASER interferometry to deduce the radial stress and hoop strain, so the maximum value achieved in each measurement is deduced. This study demonstrates the feasibility of such measurements and the interest they can represent. However, it is observed that the interfaces may degrade, even slightly, the measurements. Also, some recommendations for future tests are made:

- For hardware speed measurements, it is better to use a single block. The window material must be well known and the correction impedance that needs to be considered should be as small as possible. Indeed, this correction is well established in the case of purely uniaxial-strain loading but is not so-well known in spherical expansion.

- Regarding manganin/constantan gauges, it is preferable to use only one block on either side of the gauge and to avoid a stack of discs. This therefore implies that only one measurement is made per test. In addition, it is essential to properly center the gauge frame. These recommendations being made, the recovery tests and the post-mortem observations performed can be now presented. Indeed, the objective is to relate the maximum value of the radial stress to the observations resulting from fragments collected at the same abscissa as the abscissa of measurements.

6 Post-mortem macroscopic observations after recovery tests

In order to perform post-mortem observation of the samples with a scanning electron microscope, next to a single divergent spherical longitudinal wave test, different kinds of recovery tests are conducted: configurations are developed with the explosive in contact with a steel frame containing the alumina, whereas in other configurations the explosive is placed in contact with alumina.

The first objective of these tests is to ensure that the material could be recovered in an observable state. These tests allowed the observation of several planes perpendicular to the direction of wave propagation.

The second objective of these tests is to recover a sample only loaded by the divergent spherical compressive wave. For that, it is necessary to eliminate any interfaces in the target that could induce parasitic effects. Some steel plates are put around the target to trap the reflected tensile waves. The steel-alumina interface is removed by machining a hemispherical cavity in alumina to receive the explosive. The reflection of tensile waves in alumina is also avoided by choosing sufficiently large samples. Their dimensions are designed by numerical simulation.

These tests provide post-test observations of the damage mechanisms involved in each alumina when subjected to a divergent spherical wave. This kind of stress wave imposes to the material a one-

Handbook of Damage Mechanics; Nano to Macro Scale for Materials and Structures

Second Edition

dimensional motion in a spherical frame. This property makes easier the location and positioning of the recovered samples so the observations can be easily connected to the experimental measurements.

6.1 Macroscopic observations for coarse-grained alumina

For coarse-grained alumina, apart from the disc located near the explosive (too fragmented, powdery appearance), each disc alumina is recovered in one block. Radial cracking of these discs is visible to the naked eye (figure 10). The central area of the discs has a fragmented appearance.



Fig. 10 Coarse-grained alumina disc recovered after a preliminary spherical expansion shock wave pyrotechnic test

6.2 Macroscopic observations for fine-grained alumina

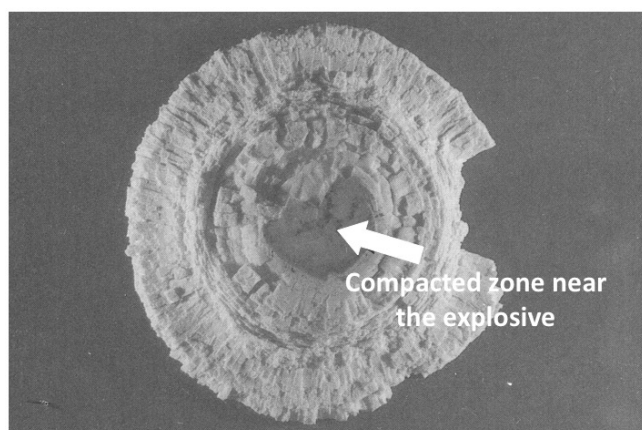


Fig. 11 Fine-grained alumina disc recovered after a preliminary spherical expansion shock wave pyrotechnic test

For fine-grained alumina, the central area that is closest to the explosive is neither fragmented nor cracked. Its color is darker than that of the material in the initial state (figure 11). As it is well-known that

Handbook of Damage Mechanics; Nano to Macro Scale for Materials and Structures

Second Edition

a very porous alumina is white and its color tends towards dark ivory when the porosity tends to zero, it can be supposed that, in this zone close to the explosive, the divergent spherical wave has densified the fine-grained alumina. This alumina seems to densify without microcracking in an area very close to the explosive

7 Post-mortem analysis with SEM microscopy

For each material, the observations are made in areas close to those where the measurements are performed. The objective pursued is to relate the observed microphysical phenomena to the stress levels reached within the material.

First, traces of plasticity phenomena (figure 12) are exhibited. Such observations are particularly unusual in quasi-static mechanical loading but in the context of high strain-rates dynamic loading and in triaxial stress states, they are more common (Hockey 1971; Lankford 1977). However, the observation of microplasticity mechanisms needs TEM analysis.

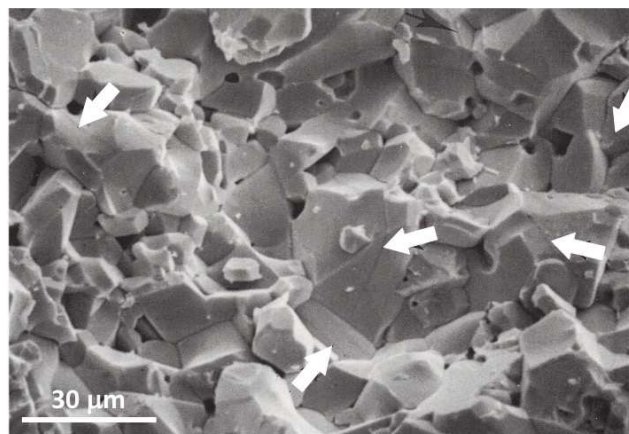


Fig. 12 SEM observations showing twinning (black arrows) in a coarse-grained alumina recovered after a divergent spherical wave test, $r \sim 25$ mm

Examination of the failure surface pattern by means of SEM microscopy shows that the cracking is completely intergranular. Some intergranular microcracks are shown. No particular site of crack nucleation can be identified. Some twins can be observed in the coarser grains (see arrows in figure 12).

7.1 SEM observations for coarse-grained alumina

The results of SEM observations are presented, considering five different abscissas where the abscissa r represents the distance between the observation locations to the center of the explosive.

Handbook of Damage Mechanics; Nano to Macro Scale for Materials and Structures

Second Edition

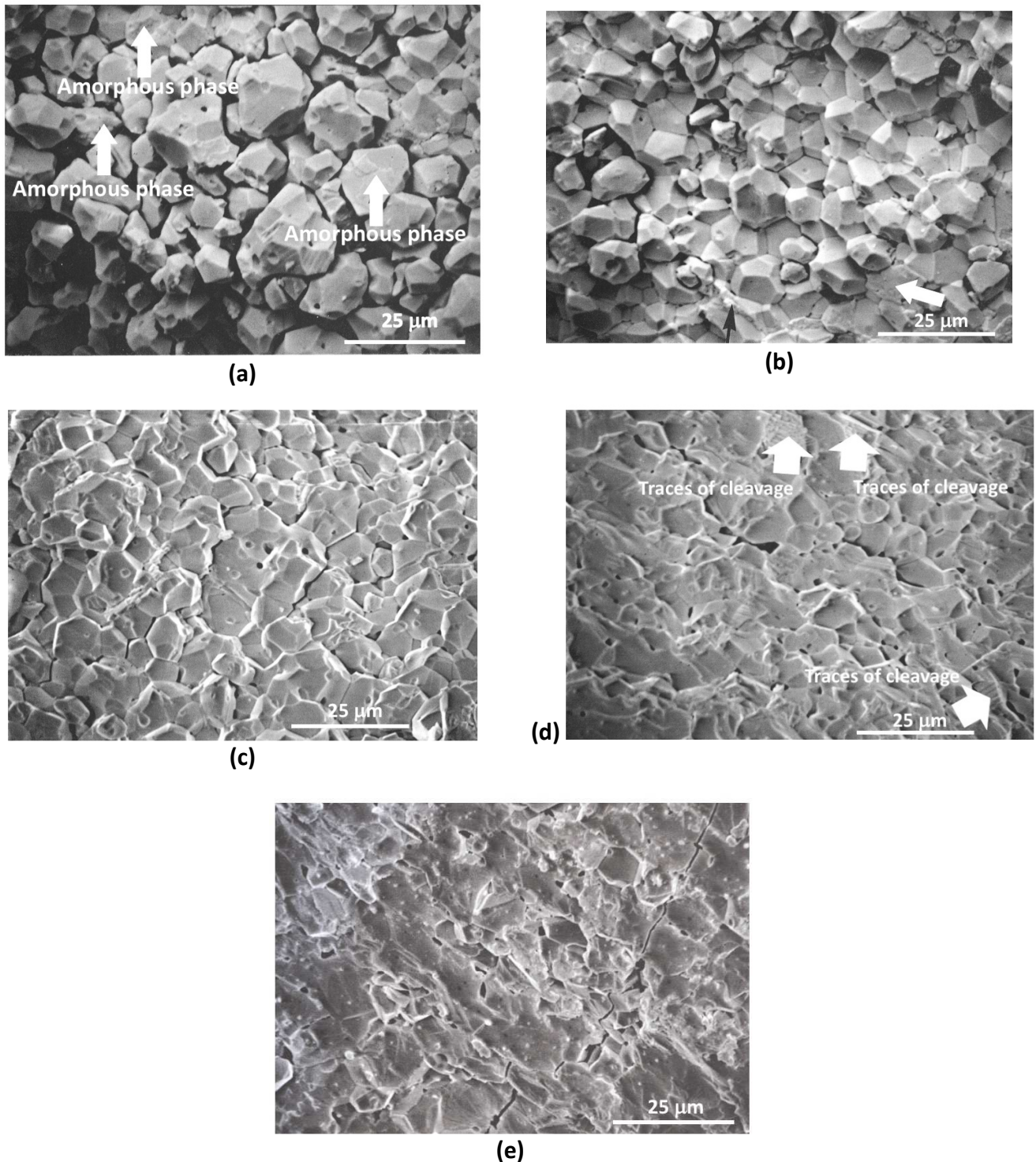


Fig. 13 SEM fractography showing intergranular failure pattern in a coarse-grained alumina recovered after a divergent spherical wave test. (a) $r = 20$ mm, (b) $r = 30$ mm, (c) $r = 35$ mm, (d) $r = 50$ mm, (e) $r = 60$ mm.

- $r = 20$ mm (figure 13a). This observation area is the closest to the explosive that is observed. The cracking pattern is completely intergranular. All the grains are separated from each other. It is possible to see traces of glassy phase (black arrows) on the faces of some grains. No transgranular microcracks are visible.

Handbook of Damage Mechanics; Nano to Macro Scale for Materials and Structures

Second Edition

- $r = 30$ mm (figure 13b): The cracking pattern is intergranular. Some grains are lost. The black arrows mark the remaining glassy phase. Some intergranular microcracks can be noted.

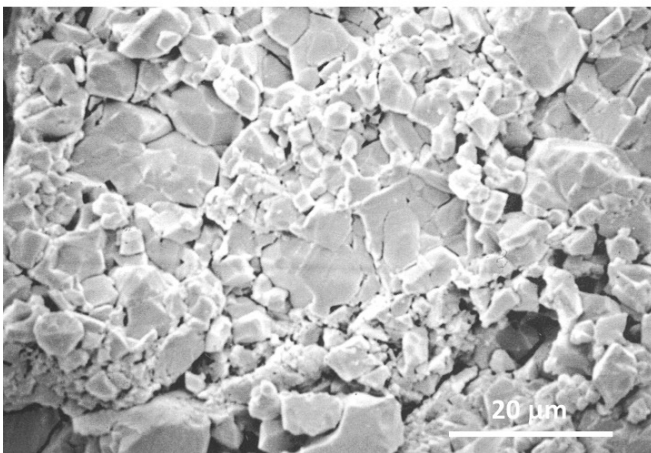
- $r = 35$ mm (figure 13c): The cracking pattern is mainly intergranular. All the grains are linked to each other. The microcracks are mainly intergranular. Microcracks of size smaller to the grain size are intergranular whereas cracks of size of the order of several grains are transgranular.

- $r = 50$ mm (figure 13d): A mixed intergranular - transgranular cracking pattern is observed. One can note the presence of cleavage marks. Cracking is mainly intergranular.

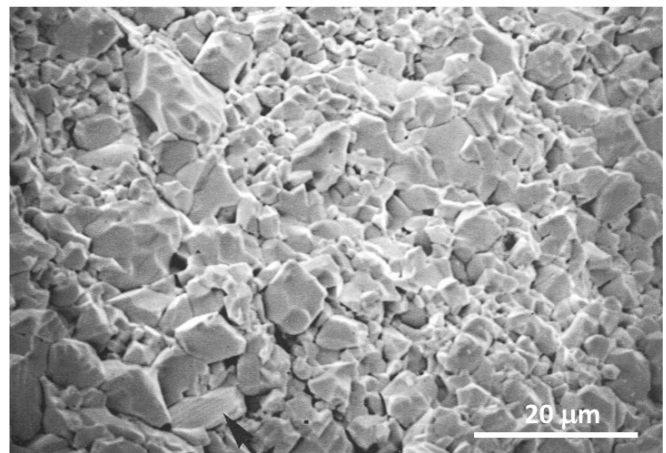
- $r = 60$ mm (figure 13e): The cracking pattern is clearly transgranular. The same observations are made for abscissa much further from the explosive. These cracks are induced by the tensile hoop stresses.

7.2 SEM observations for fine-grained alumina

Like what has been presented for coarse grain alumina, the results of observations made in the case of fine-grained alumina for five abscissas exhibit very different phenomena (Fig. 14). Each of them is representative of different radius r (r is the distance between the observation location to the center of the explosive).



(a)



(b)

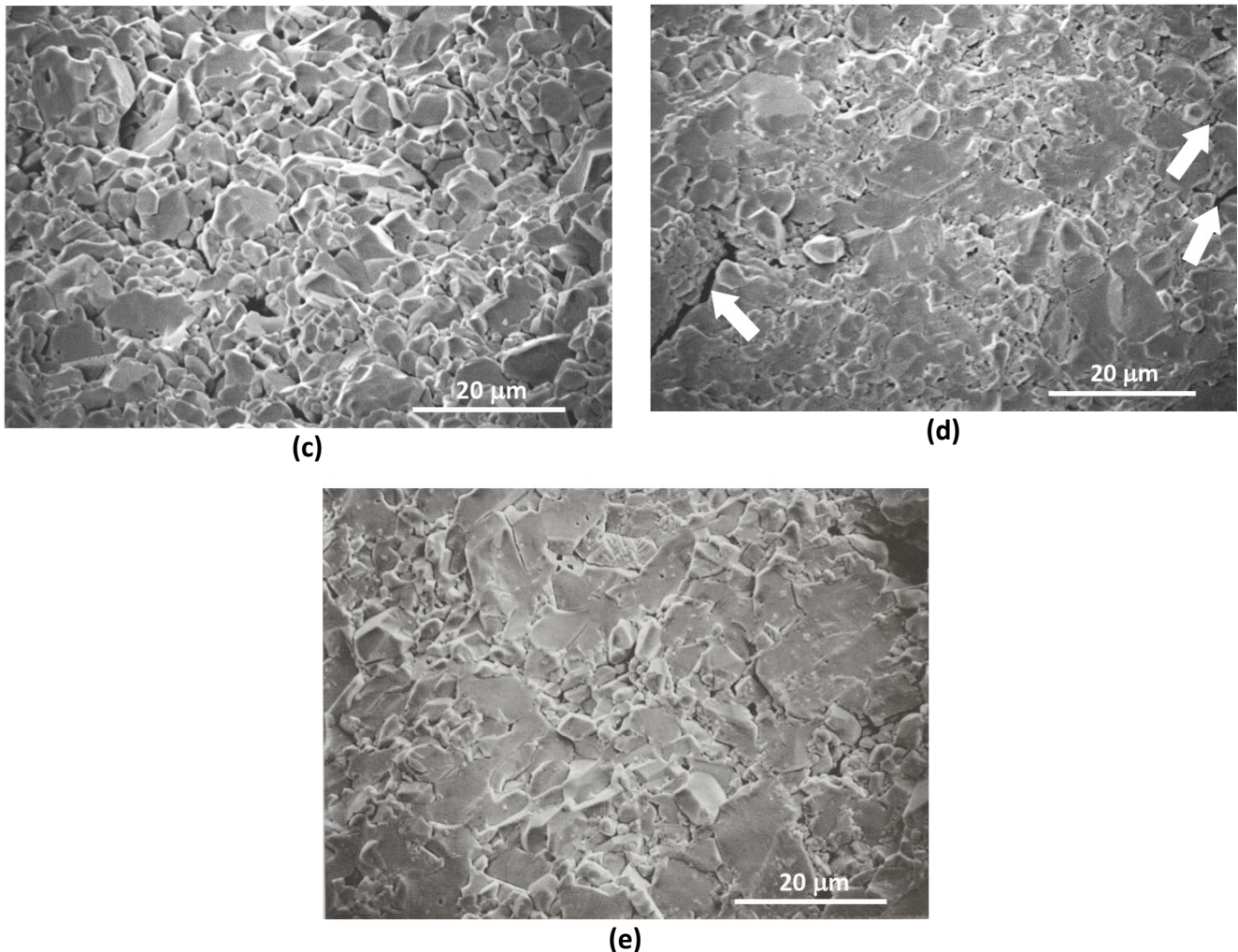


Fig. 14 SEM fractography showing the failure pattern in a fine-grained alumina recovered after a divergent spherical wave test. (a) $r = 20$ mm, (b) $r = 25$ mm, (c) $r = 40$ mm, (d) $r = 50$ mm, (e) $r = 70$ mm.

- $r = 20$ mm (figure 14a): The failure pattern shows intergranular cracking. Many grains are separated. In the center, that the material seems to be compacted and transgranular cracks are exhibited. The pattern are much less homogeneous than in the case of alumina AL23.

- $r = 25$ mm (figure 14b): The failure pattern is intergranular. This fractography shows some microcracks and intergranular cracks. Few grains are separated. The black arrow indicates a grain that looks twinned. Transmission electron microscope observations should provide more specific answers.

- $r = 40$ mm (figure 14c): The failure pattern is completely intergranular. This fractography shows the presence of some cracks intergranular. These cracks seem to be more open at the places where the heterogeneity of grain size is more marked.

Handbook of Damage Mechanics; Nano to Macro Scale for Materials and Structures

Second Edition

- $r = 50$ mm (figure 14d): The previous remark is even better illustrated by this fractography. Here the pattern has become mainly transgranular. Some intergranular cracks remain visible (black arrows).

- $r = 70$ mm (figure 14e): The pattern is fully transgranular. Note the presence of cleavage marks and intergranular cracks. These cracks are preferentially located around the large pores and the smaller grains.

8 Post-mortem analysis with TEM microscopy

The aim of this analysis is to answer qualitatively to the following questions: - Do microplastic phenomena really exist in the alumina loaded under such high pressure and high strain rates? Where these mechanisms take place and what is the nature of these mechanisms? To answer to these questions, several observations are performed considering small abscissas.

8.1 TEM observations for coarse-grained alumina

Given the observations made by SEM microscopy, the number of observations by TEM microscopy is reduced to only three abscissas (Fig. 15).

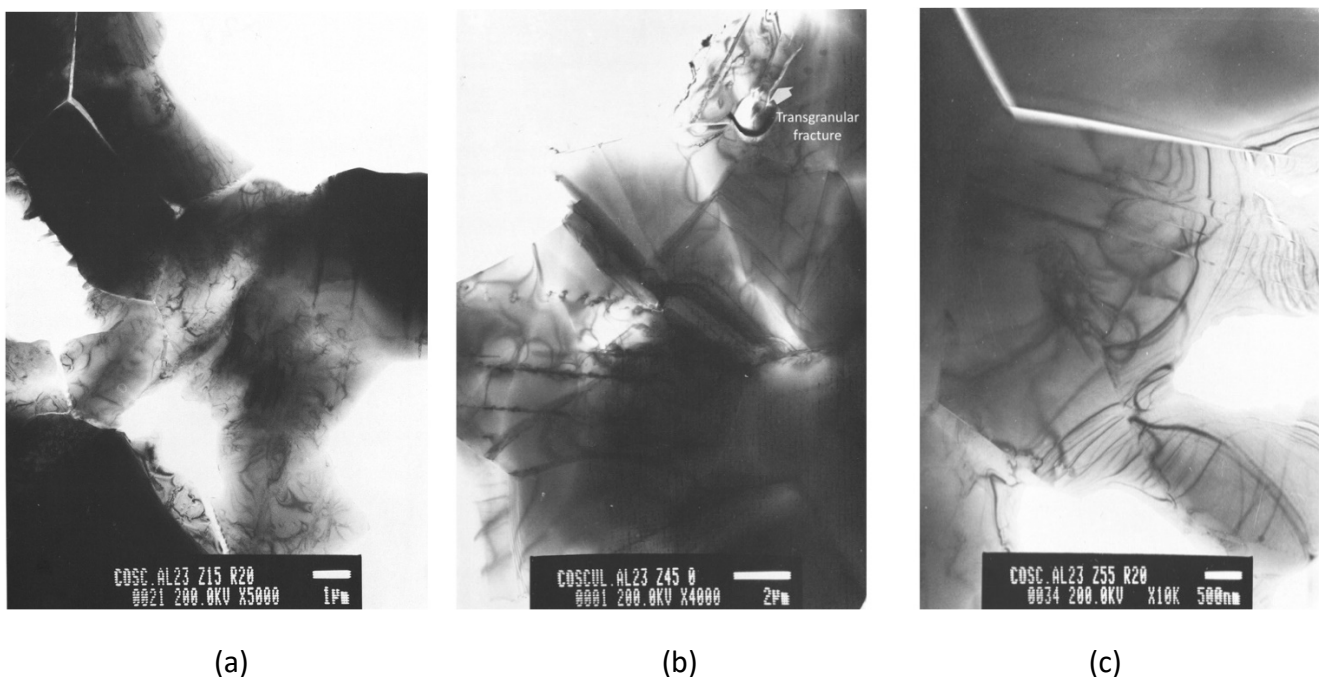


Fig. 15 TEM observations of coarse-grained alumina recovered after a divergent spherical wave behavior test. (a) $r = 25$ mm, (b) $r = 45$ mm, the arrow shows a transgranular microcrack from a pore and not connected with the grain seal, (c) $r = 58$ mm.

- $r = 25$ mm (figure 15a): Very close to the explosive, microplastic phenomena are very numerous (twins, dislocations). The picture also shows a network of intergranular microcracks. The micrographs show at the grain boundaries, residues of glassy phase. Otherwise, it seems that the microcracks appear preferentially near the most microplasticized grains.

Handbook of Damage Mechanics; Nano to Macro Scale for Materials and Structures

Second Edition

- $r = 45$ mm (figure 15b): Microplastic activity is much less important. It is reduced to a few dislocation movements observed on part of the grains (approximately 50%). The picture shows a presence of a transgranular microcracks. But this phenomenon is not representative of all the observations performed (Coscolluela, 1992). Some rare intergranular microcracks are observed.

- $r = 58$ mm (figure 15c): Microplastic activity is relatively a little less to what has been observed for the abscissa previous. The micrograph exhibits an intergranular microcrack. The black curves represent fringes of shapes.

8.2 TEM observations for fine-grained alumina

Like coarse-grained alumina, the aim is not to perform a TEM study proper on fine-grained alumina. The results of the observations are only intended to help us describe physical phenomena in a way that understand mechanical behavior.

Based on the results obtained at the SEM, only three abscissas are selected for TEM observations:

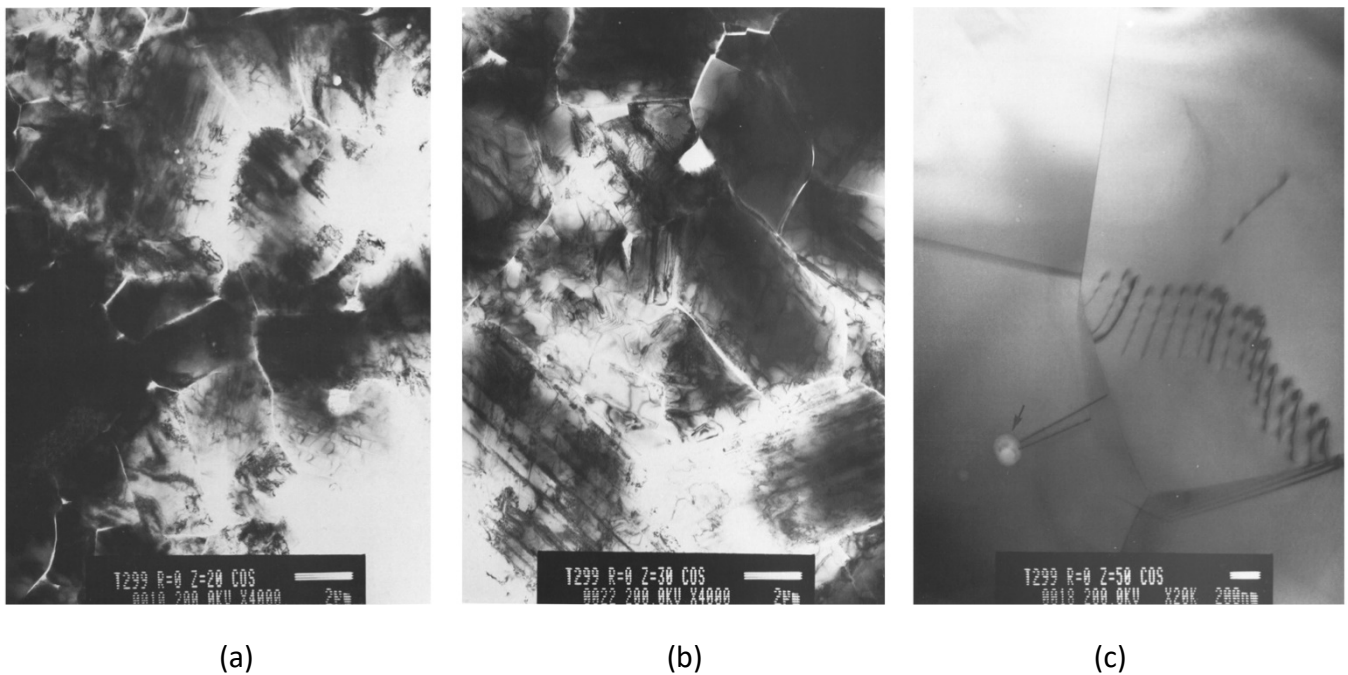


Fig. 16 TEM observations of fine-grained alumina recovered after a divergent spherical wave test. (a) $r = 20$ mm, (b) $r = 30$ mm, (c) $r = 50$ mm, the arrow indicates an intragranular pore.

- $r = 20$ mm (figure 16a): Near the explosive, the microplasticity activity is very important. Most of grains exhibit dislocations and twins. Micrographs show (white lines) an important network of intergranular microcracks. Additional observations made it possible to find that this network is dense and not oriented. The density of microcracks is not more prominent in the most microplasticized areas. These microcracks seem to be wider when they are next to the larger grains.

Handbook of Damage Mechanics; Nano to Macro Scale for Materials and Structures

Second Edition

- $r = 30$ mm (figure 16b): Microplasticity activity is still very important. Alumina is the seat of the same physical phenomena than at the previous abscissa with a decrease in the densities of microcracks and twins. However, the relationship between microplasticity and microcracking remains difficult to establish.

- $r = 50$ mm (figure 16c): The observations made at this abscissa show the absence of intergranular microcracks. Microplasticity activity has almost disappeared even if few dislocations stacks are still observed.

9 Discussion about the physical phenomena

9.1 Analysis of microscopic observations

The purpose of the recovery tests is to conduct a post-mortem analysis of a material which is only subjected to a divergent spherical wave loading. All parasitic effects must be eliminated to make the observations valid. The experimental setup that is best suited to this problem is the test with one bloc alumina. In the case of the fine-grained alumina, the steel confinement of the preliminary tests allowed the observation of a compacted area without micro-cracking network.

A single divergent spherical expansion test allows observing several very different phenomena. This is related to the divergent nature of the spherical wave. Many observations are common to the two alumina: - diffuse damage, - transition from an intergranular failure pattern to a transgranular failure pattern away farther from the explosive, - radial cracking network, oriented fragmentation and the increase of the fragments size far from the explosive (tensile damage).

The important difference between the two alumina lies in the nature of the area fragmented close to the explosive:

- In the case of coarse-grained alumina, all of the grains are separated from each other, so the fragments take on the appearance of a powder.

- In the case of fine-grained alumina, this phenomenon also appears but is much less pronounced.

To synthesize the results obtained by the measurement tests and recovery tests, for each characteristic abscissa, the maximum stress measured is related to the observations performed using SEM and TEM techniques (figures 17 and 18).

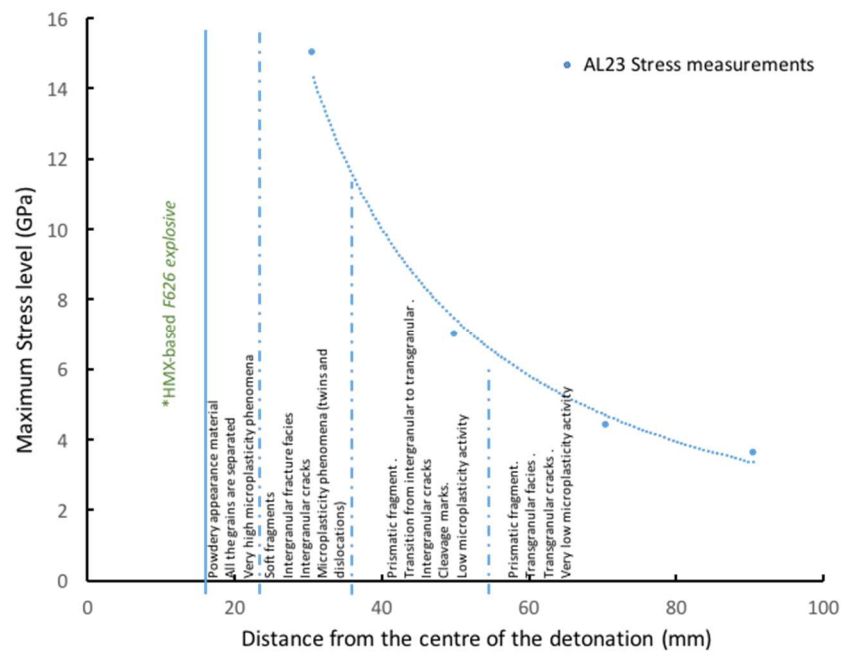


Fig. 17 Synthesis of the physical phenomena observed from a recovered coarse-grained alumina loaded by a divergent spherical wave

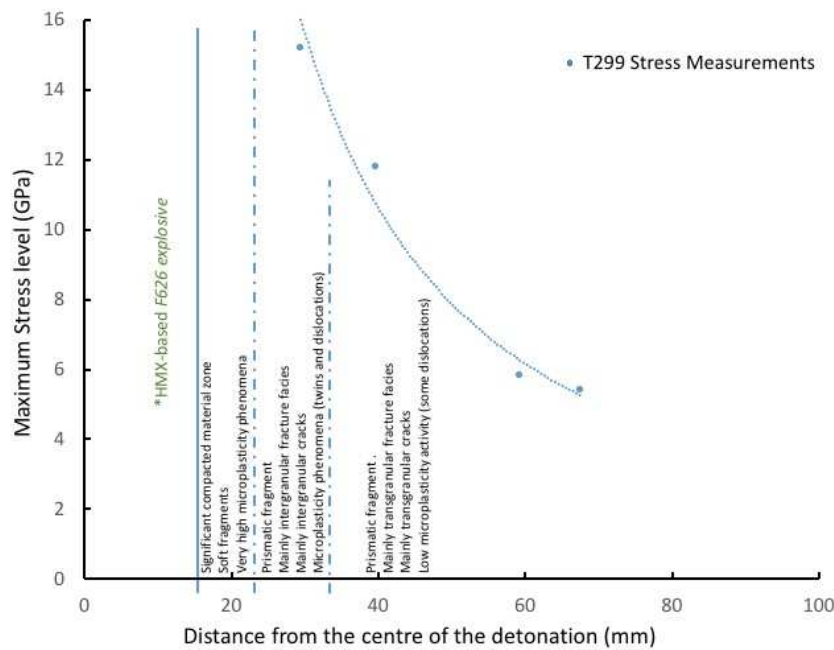


Fig. 18 Synthesis of the physical phenomena observed from a recovered fine-grained alumina loaded by a divergent spherical wave

Handbook of Damage Mechanics; Nano to Macro Scale for Materials and Structures

Second Edition

Several comments can be made regarding these divergent spherical expansion tests: - The values of the stresses provided are more precise in the case of the fine-grained alumina (T299). Indeed, the stresses are derived from measurements by stress-gauges. In the case of coarse-grained alumina (AL23), the stresses are calculated from the IDL velocity signals. For this, it is assumed that the level of maximum compression takes place according to a uniaxial strain path. The numerical simulations show that this is not entirely true. In the figures 17 and 18, the positions of the boundaries separating two physical phenomena does not represent a significant discontinuity according the above observations. For AL23 alumina, there is a rapid decrease in damage with the abscissa due to a fast decrease of maximum level of stress. - For T299 alumina, this same phenomenon appears. But, in this case, the transition between both mechanisms is much closer to the center of the explosive. In addition, there is no area where all the grains are completely separated. Therefore, to cause equivalent damage, the necessary stress level would be much greater in the case of fine-grained alumina.

9.2 Influence of microstructural parameters

The three microstructural parameters which mainly influence the dynamic behavior of alumina are the glassy phase, the porosity and the grain size.

Throughout the stresses space, the role of the *glassy phase* is the same. Indeed, it is always linked to cracking phenomena (Moya et al. 1981). When the percentage of this amorphous phase is low (6%), it hardly changes the elastic characteristics of the alumina.

As regards to the plastic behavior in uniaxial-strain compression, the results obtained by Longy (1987) on a 94% pure alumina, show that the Hugoniot Elastic Limit (HEL) is not affected by the presence of the *glassy phase*. On the other hand, this intergranular phase is at the origin of the appearance of intergranular cracks in alumina in triaxial compression (Yeshurun et al. 1989; Longy 1987).

Porosity plays a major role in the domain of the stresses between the uniaxial compressive strain axis and the uniaxial compressive stress axis (Fig. 3). The measurements and observations made in several works (Knudsen 1962; Wachtman Jr. 1969; Cosculluela 1992), show that the increase in *porosity* reduces the elastic moduli and the tensile strength of the alumina. Intergranular pores are generally the sites of cracks nucleation.

In triaxial compressive state, the low *porosity* does not modify the microplasticity activity of pure alumina. Plastic deformation of the grains induces a compaction of the porous structure. This compaction is accompanied by damage which begins for levels of stresses that do not dependent on the initial porosity of the material. In this case, the elastic limit of Hugoniot (H.E.L) corresponds to the coupling between the pores collapse and the microplasticity activity. A reduction of the porosity induces an increase of the elastic moduli and of the elastic limit (HEL) of the alumina.

So, the H.E.L., depends on the initial *porosity* of alumina (Gust and Royce, 1971) according to a relation:

$$\sigma_{HEL} = \sigma_0 e^{-bp} \quad (\text{Eq. 13})$$

Handbook of Damage Mechanics; Nano to Macro Scale for Materials and Structures

Second Edition

where p is the initial porosity and $\bar{\sigma}_0$, b are material parameters.

To accommodate the excessive strain that is imposed to the material loaded in divergent spherical wave test, the material (even ceramics) must develop plasticity or microcracking to dissipate the excessive energy. The results obtained from the plate impact tests and divergent spherical expansion tests show that *small grain alumina plasticizes without microcracking* up to 12 GPa. This mode of energy dissipation seems to be related to the small grain size. Therefore, energy dissipation by microcracking in fine-grained alumina takes place for higher pressure levels with shear deformation mode.

In the case of small grain alumina (A 16-2), fracturing corresponds to a tensile transgranular cracking far from the explosive. In the case of large grain alumina (AL23) the orientation of the cracks depends on the triaxiality level of stresses: whereas, the fracturing is transgranular far from the explosive (tensile damage); it is intergranular closer to the explosive (compression damage). Far from explosive, the orientation of the cracks remains parallel to the radial direction.

Finally, the *influence of the grain size is stronger* in the zone where the intergranular cracking occurs. In both aluminas, the tensile fracturing is transgranular. The cracks propagate perpendicularly to the direction of maximum traction (hoop direction).

Closer to the explosive compression stresses are supposed to initiate damage which comes from the existence of local shear stresses due to the heterogeneities in the materials (difference between the grain size, grain orientation and porosities). These cracks then propagate parallel to the direction of compression.

For fine-grained alumina, transgranular fracturing is restricted to uniaxial compression stress state. A weak triaxiality state of the stresses seem to inhibit this kind of damage. The compaction phase is due to microplastic deformation of the grains. Microcracks only appear for very high stress levels in uniaxial contraction (> 12 GPa).

Compared to this behavior, the enlargement of the grains has two consequences:

- The formation of intergranular cracks near the explosive, where the triaxiality state of the stresses is high. Intergranular damage can be due to a weakening of the grain boundaries due to a relatively greater thickness of the secondary phase in coarse grain alumina and a more marked anisotropy of the deformation in the case of coarse-grained alumina, therefore *higher local shear stresses*.
 - A reduction in the microplasticity threshold and compaction of alumina. Indeed, the Hugoniot Elastic Limit depends on the size of the grains according to the Petch's law (1953). A micromechanical justification is given by the dislocation theory applied to polycrystalline solids.
-

Handbook of Damage Mechanics; Nano to Macro Scale for Materials and Structures

Second Edition

10 Conclusion

The aim of this chapter is to understand to what extent the microstructural parameters are responsible for cracking and microplasticity mechanisms in the aluminas during a loading by a divergent spherical wave. The studied stress history is representative of the first moments of the interaction between a projectile and an alumina armor shield. The role of each microstructural parameter (glassy phase, porosity, grain size) during this short time phase can be identified. Different microstructural phenomena are highlighted. During the triaxial compression phase, for very dense ceramics, the two microstructural parameters which conditioned the microcracking of the aluminas are the vitreous phase and the grain size. Too large glass phase percentage ($> 1\%$) leads to a microcracking of this phase. An increase in grain size lowers the nucleation threshold of microcracks. The latter are generated at the grain boundaries by local shear stresses proportional to the grain size. In addition, for an equal percentage of vitreous phase, the thickness of this glassy phase at the grain boundaries is greater in coarse grain alumina, which weakens the grain boundary.

A similarity exists between the increase of the grains size on the one hand and the increase of percentage of glassy phase on the other hand.

During the relaxation phase, micro-cracks nucleated in triaxial compression loading stage then become potential defects in the same way as the pores. The activation of these defects takes place only when the state of compression ceases to be triaxial.

This study made it possible to highlight and understand the phenomena involved in aluminas when they are stressed by a divergent spherical wave. According to the observations made in the present study it can be concluded that, for armor application, it would be better using pure ceramic (purity $> 99.5\%$), with high density (for alumina $\rho > 3.8 \text{ g.cm}^{-3}$) and fine-grained polycrystalline alumina ($d < 5 \mu\text{m}$).

The pyrotechnic divergent spherical wave experimental technique can be applied to any kinds of brittle materials in general. The influence of microstructural parameters can be transposed to other polycrystalline ceramics.

Handbook of Damage Mechanics; Nano to Macro Scale for Materials and Structures

Second Edition

References

- A. V. Andriyash and al., Long-term evolution of spherical shell with boron carbide layer after explosive compression. *J. Appl. Phys.* **126**, 085903 (2019)
- F.G. Blake Jr., Spherical wave propagation in solid media. *J. Acoust. Amer. Soc.* **24**, 211-215 (1952)
- S.J. Bless, N.S. Brar, Z. Rosenberg, Failure of ceramic and glass rods under dynamic compression, in *Proceedings of the American Physical Society Topical Conference, Shock Compression of Condensed Matter*, Albuquerque 1989, pp. 939-942. Edited by S.C. Schmidt, J.N. Johnson, L.W. Davison, North Holland (1990)
- J. Cagnoux, J., A. Cosculluela, Influence of grain-size on triaxial dynamic behavior of alumina, in *Proceedings of the International Seminar on Dynamic Failure of materials : theory, experiments and numerics*, Technische Universität Wien, 2-4 Jan., pp73-84, Ed. By H.P. Rossmannith and A.J. Rosakis (1991)
- A. Cosculluela, Plasticité, endommagements et ruptures des alumines sous sollicitations dynamiques triaxiales : influence de la taille des grains (Ph.D. dissertation), University of Bordeaux, France (1992)
- A. Cosculluela, J. Cagnoux, F. Collombet, Uniaxial compression of alumina : structure, microstructure and strain rate, in *Proceedings of 3rd DYMAT Conference*, 1991, Strasbourg, France, pp.109-116, Les Editions de Physique (1991a)
- A. Cosculluela, J. Cagnoux, F. Collombet, Two types of experiments for studying uniaxial dynamic compression of alumina, in *Proceedings of the American Physical Society Topical Conference*, Williamsburg (1991b)
- A.G. Evans, Y. Fu, The mechanical behavior of alumina : a model anisotropic brittle solid, in *Fracture in Ceramics Materials* - Ed. by Evans, Noyes Publications, Park Ridge, NJ (1984)
- P. Forquin, L. Tran, P-F. Louvigné, L. Rota, F. Hild, Effect of aluminum reinforcement on the dynamic fragmentation of SiC ceramics, *Int. J. Impact Eng.*, **28**, 1061-1076 (2003)
- M.L. Ghosh, On the propagation of spherical waves due to large underground explosions. *Pure Appl. Geophys.* **72**, pp 22-34 (1969)
- W.H. Gust, E.B. Royce, Dynamic Yield Of B4C, BeO and Al₂O₃ Ceramics, *J. Appl. Phys.*, 42 (1), pp. 276 (1971)
- F.E. Heuze et al., Explosion phenomenology in jointed rocks. In *Explosion source phenomenology, geophysical monograph 65*, ed. by Taylor SR, Patton HJ, Richards PG, American Geophysical Union, Washington DC, pp 253–260 (1991)
-

Handbook of Damage Mechanics; Nano to Macro Scale for Materials and Structures

Second Edition

B.J. Hockey, Plastic Deformation of Aluminum Oxide by Indentation and Abrasion, *J. Am. Ceram. Soc.* 54 (1971) 223–231. <https://doi.org/10.1111/j.1151-2916.1971.tb12277.x>.

D.G. Howitt, P.V. Kelsey, Dislocation microstructure of shock-loaded Alumina, in *Proceeding of the International Conference on Impact Loading and Dynamic Behavior of Materials*, Bremen, FRG, (1987), pp. 249-256, Ed. by C.Y. Chiem, H.D. Kunze, L.W. Meyer, DGM Informationsgesellschaft MbH, Oberursels, FRG (1988)

F.P. Knudsen, Effect of porosity on Young modulus of Alumina, *J. Am. Ceram. Soc.*, **45**, 2, pp. 94-95 (1962)

J. Lankford, Compressive strength and microplasticity in polycrystalline alumina, *J. Mater. Sci.* 12 (1977) 791–796. <https://doi.org/10.1007/BF00548172>.

F. Longy, Déformation et endommagement de céramiques soumises à un choc intense : aspects macro et micromécaniques (Ph.D. dissertation) (University of Limoges, Bordeaux, 1992)

L.H. Louro, M.A. Meyers, Effect of stress State and microstructural parameters on impact damage of alumina-based ceramics. *J. of Mater. Science* **24**, pp. 2516-2532 (1989)

J.S. Moya, W.H. Kriven and J.A. Pask, Influence of grain boundary silica impurity on alumina toughness, in *Proceedings of the 17th Conf. on ceramics*, 1981, pp 317-322

N.J. Petch, *J. Iron Steel Inst.*, London, **174**, pp. 25-28 (1953)

P. Riou, C. Denoual, C.E. Cottenot, Visualization of the damage evolution in impacted silicon carbide ceramics, *Int. J. Impact Eng.*, 21 (4), 225-235 (1998)

S. Satapathy, Dynamic spherical cavity expansion in brittle ceramics. *Int. J. of Solids and Structures* **38**, pp 5833-5845 (2001)

Y. Yeshurun et al., The Dynamic Shear Strength of shock-loaded two-phase ceramics, in *Proceedings of the Fourth International Conference on the Mechanical Properties of Materials at High Rates of Strain*, Oxford, 19–22 March, ed. by J. Harding, Inst. Physics Pub. Div., Bristol (1989)

J.B. Wachtman, Elastic deformation of ceramics and other refractory metals, in *proceedings of the Symposium Mechanical and Thermal Properties of Ceramics*, Gaithersburg, April1-2, 1968. Ed. By J.B. Wachtman Jr, National Bureau of Standards, Washington DC (1969)

Index Terms

Handbook of Damage Mechanics; Nano to Macro Scale for Materials and Structures

Second Edition

Alumina

Bilayered-armor

Divergent spherical wave

Dynamic behavior

High-strain-rate

HMX based F626

Manganin/constantan gauges

Microplasticity

Microcracks

Scanning Electron Microscopy

Spherical expansion shock wave pyrotechnic test

Transmission Electron Microscopy

Handbook of Damage Mechanics; Nano to Macro Scale for Materials and Structures

Second Edition

Table des matières

1	<i>Introduction</i>	2
2	<i>Description of the problem</i>	2
3	<i>State of the art and position of the problem for the divergent spherical wave test</i>	5
4	<i>Numerical investigation of the loading history</i>	6
4.1	Elastic behavior hypothesis	7
4.2	Elastic perfectly plastic behavior hypothesis	8
5	<i>Experiments performed on two alumina ceramics</i>	11
5.1	Presentation of the two alumina ceramics.....	11
5.2	Experimental set-up and instrumentation	12
5.3	Experimental results obtained with coarse-grained alumina AL23	13
5.4	Experimental results obtained with fine-grained alumina T299	14
5.5	Discussion on the experimental results	17
6	<i>Post-mortem macroscopic observations after recovery tests</i>	17
6.1	Macroscopic observations for coarse-grained alumina.....	18
6.2	Macroscopic observations for fine-grained alumina.....	18
7	<i>Post-mortem analysis with SEM microscopy</i>	19
7.1	SEM observations for coarse-grained alumina	19
7.2	SEM observations for fine-grained alumina	21
8	<i>Post-mortem analysis with TEM microscopy</i>	23
8.1	TEM observations for coarse-grained alumina	23
8.2	TEM observations for fine-grained alumina	24
9	<i>Discussion about the physical phenomena</i>	25
9.1	Analysis of microscopic observations.....	25
9.2	Influence of microstructural parameters	27
10	<i>Conclusion</i>	29

Handbook of Damage Mechanics; Nano to Macro Scale for Materials and Structures

Second Edition

Figures:

FIG. 1 STATES OF STRESSES IMPOSED ON AN ELEMENT OF VOLUME BY A DIVERGENT SPHERICAL WAVE.....	4
FIG. 2 LOADING PATH IMPOSED BY A DIVERGENT SPHERICAL WAVE TO AN ELASTIC MATERIAL.....	4
FIG. 3 LOADING PATH APPLIED TO A MATERIAL LOADING AT THREE DIFFERENT ABCISSAS.....	6
FIG. 4 NUMERICAL SIMULATION OF THE LOADING PATH IMPOSED BY A DIVERGENT SPHERICAL WAVE TO AN ELASTIC MATERIAL.....	8
FIG. 5 NUMERICAL SIMULATION OF A DIVERGENT SPHERICAL WAVE CONSIDERING AN ELASTOPLASTIC BEHAVIOR FOR THE CERAMIC MATERIAL. (A) RADIAL PARTICLE VELOCITY VERSUS TIME, (B) RADIAL STRESS VERSUS TIME, (C) RADIAL STRESS VERSUS HOOP STRESS.	10
FIG. 6 EXPERIMENTAL SET-UP DEDICATED TO THE MATERIAL VELOCITY MEASUREMENTS AT THE REAR FACE OF THE MATERIAL LOADED BY A DIVERGENT SPHERICAL WAVE	12
FIG. 7 VELOCITY PROFILE AT THE AL23 ALUMINA-PMMA INTERFACE FOR DIFFERENT DISTANCES FROM THE CENTER OF THE DETONATION.....	13
FIG. 8 PROFILE OF THE T299 ALUMINA-PMMA INTERFACE VELOCITY FOR DIFFERENT DISTANCES FROM THE CENTER OF THE DETONATION	15
FIG. 9 PROFILE OF THE RADIAL STRESS FOR DIFFERENT DISTANCES FROM THE CENTER OF THE DETONATION.....	16
FIG. 10 COARSE-GRAINED ALUMINA DISC RECOVERED AFTER A PRELIMINARY SPHERICAL EXPANSION SHOCK WAVE PYROTECHNIC TEST.....	18
FIG. 11 FINE-GRAINED ALUMINA DISC RECOVERED AFTER A PRELIMINARY SPHERICAL EXPANSION SHOCK WAVE PYROTECHNIC TEST	18
FIG. 12 SEM OBSERVATIONS SHOWING TWINNING (BLACK ARROWS) IN A COARSE-GRAINED ALUMINA RECOVERED AFTER A DIVERGENT SPHERICAL WAVE TEST, $R \sim 25$ MM.....	19
FIG. 13 SEM FRACTOGRAPHY SHOWING INTERGRANULAR FAILURE PATTERN IN A COARSE-GRAINED ALUMINA RECOVERED AFTER A DIVERGENT SPHERICAL WAVE TEST. (A) $R = 20$ MM, (B) $R = 30$ MM, (C) $R = 35$ MM, (D) $R = 50$ MM, (E) $R = 60$ MM.	20
FIG. 14 SEM FRACTOGRAPHY SHOWING THE FAILURE PATTERN IN A FINE-GRAINED ALUMINA RECOVERED AFTER A DIVERGENT SPHERICAL WAVE TEST. (A) $R = 20$ MM, (B) $R = 25$ MM, (C) $R = 40$ MM, (D) $R = 50$ MM, (E) $R = 70$ MM.....	22
FIG. 15 TEM OBSERVATIONS OF COARSE-GRAINED ALUMINA RECOVERED AFTER A DIVERGENT SPHERICAL WAVE BEHAVIOR TEST. (A) $R = 25$ MM, (B) $R = 45$ MM, THE ARROW SHOWS A TRANSGRANULAR MICROCRACK FROM A PORE AND NOT CONNECTED WITH THE GRAIN SEAL, (C) $R = 58$ MM. ...	23
FIG. 16 TEM OBSERVATIONS OF FINE-GRAINED ALUMINA RECOVERED AFTER A DIVERGENT SPHERICAL WAVE TEST. (A) $R = 20$ MM, (B) $R = 30$ MM, (C) $R = 50$ MM, THE ARROW INDICATES AN INTRAGRANULAR PORE.	24
FIG. 17 SYNTHESIS OF THE PHYSICAL PHENOMENA OBSERVED FROM A RECOVERED COARSE-GRAINED ALUMINA LOADED BY A DIVERGENT SPHERICAL WAVE	26
FIG. 18 SYNTHESIS OF THE PHYSICAL PHENOMENA OBSERVED FROM A RECOVERED FINE-GRAINED ALUMINA LOADED BY A DIVERGENT SPHERICAL WAVE	26

Tables:

TABLE 1 PHYSICAL PROPERTIES OF MATERIALS USED IN THIS EXPERIMENTAL STUDY (UNCERTAINTIES: 7%).....	12
TABLE 2 MAXIMAL VALUES OF ALUMINA-PMMA INTERFACE VELOCITY AND ESTIMATED ASSOCIATED STRESSES (UNCERTAINTIES:15%).....	16